Technical Note: Two types of absolute dynamic ocean topography

Peter C. Chu

Naval Ocean Analysis and Prediction Laboratory, Department of Oceanography
Naval Postgraduate School, Monterey, CA 93943, USA

Correspondence to: Peter C. Chu (pcchu@nps.edu)

Abstract. Two types of marine geoid exist with the first type to be the *average level of sea surface height (SSH) if the* **water is at rest** (classical definition), and the second type to be satellite determined with the condition that *the water is* ***usually not at rest***. Differences between the two are exclusion (inclusion) of the gravity anomaly and non-measurable (measurable) in the first (second) type. The associated *absolute dynamic ocean topography* (referred as DOT), i.e., SSH minus marine geoid, also has two types. Horizontal gradients of the first type DOT represent the absolute surface geostrophic currents due to water at rest on the first type marine geoid. Horizontal gradients of the second type DOT represent the surface geostrophic currents relative to the second type marine geoid due to water not at rest there. Difference between the two is quantitatively identified in this note through comparison between the first type DOT and the mean second type DOT (MDOT). The first type DOT is determined by a physical principle that the geostrophic balance takes the minimum energy state. Based on that, a new elliptic equation is derived for the first type DOT. Continuation of geoid from land to ocean leads to an inhomogeneous Dirichlet boundary condition with the boundary values taking satellite observed second type MDOT. This well-posed elliptic equation is integrated numerically on 1° grids for the world oceans with the forcing function computed from the World Ocean Atlas (T, S) fields and the sea-floor topography obtained from the NOAA's ETOPO5 model. Between the first type DOT

and second type MDOT, the relative root-mean square (RMS) difference (versus RMS of the first type DOT) is 38.6% and the RMS difference of the horizontal gradients (versus

30   RMS of the horizontal gradient of the first type DOT) is near 100%. The standard deviation of horizontal gradients of DOT is nearly twice larger for the second type (satellite determined marine geoid with gravity anomaly) than for the first type (geostrophic balance without gravity anomaly). Such difference needs further attention from oceanographic and geodetic communities, especially the oceanographic representation of the horizontal

35   gradients of the second type MDOT (***not the absolute surface geostrophic currents***).

1. Introduction

Let the coordinates (x, y, z) be in zonal, latitudinal, and vertical directions. The a*bsolute dynamic ocean topography* (hereafter referred as DOT) $\hat{D}$ is the sea surface height (SSH) (waves and tides filtered out) relative to the marine geoid (i.e., the equipotential surface),

40
$$\hat{D} = S - \hat{N} , \tag{1}$$

where S is the SSH; $\hat{N}$ is the marine geoid height above to the reference ellipsoid (Fig. 1). $\hat{D}$ is an important signal in oceanography; and $\hat{N}$ is of prime interest in geodesy. Eq. (1) is also applicable if defined relative to the center of the Earth. The geoid height $\hat{N}(x, y)$ and other associated measurable quantities such as gravity anomaly $\Delta g(x, y)$ are

45   related to the anomaly of the gravitational potential $V(x, y, z)$ to a first approximation by the well-known Brun's formula (e.g., Hofmann-Wellenhof and Moritz, 2005),

$$\hat{N}(x, y) = \frac{V(x, y, 0)}{g} , \tag{2}$$

where $g = 9.81$ m/s^2, is the globally mean normal gravity, which is usually represented by g_0 in geodesy. The gravity anomaly is the vertical derivative of the potential

50
$$\Delta g(x,y) = -\frac{\partial V(x,y,0)}{\partial z} \ ,$$
(3)

where the anomaly of the gravity potential V satisfies the Laplace equation

$$\frac{\partial^2 V}{\partial x^2} + \frac{\partial^2 V}{\partial y^2} + \frac{\partial^2 V}{\partial z^2} = 0 \ .$$
(4)

The vertical deflection is the slope of the geoid

$$\frac{\partial \hat{N}}{\partial x} = \frac{1}{g}\frac{\partial V}{\partial x}, \quad \frac{\partial \hat{N}}{\partial y} = \frac{1}{g}\frac{\partial V}{\partial y}$$
(5)

55   which connects to the gravity anomaly by

$$\frac{\partial(\Delta g)}{\partial z} = g\left(\frac{\partial^2 \hat{N}}{\partial x^2} + \frac{\partial^2 \hat{N}}{\partial y^2}\right)$$
(6)

Eq(6) links the vertical gravity gradient to the horizontal Laplacian of the marine geoid

height $\hat{N}$ and serves as the basic principle in the satellite marine geodesy. Since $\hat{D}$ is the

difference of the two large fields S and $\hat{N}$ (two orders of magnitude larger than $\hat{D}$), it is

60   extremely sensitive to any error in either S or $\hat{N}$ – even 1% error in either field can lead

to error in $\hat{D}$ that is of the same order of magnitudes as $\hat{D}$ itself (Wunsch and Gaposchkin,

1980; Bingham et al., 2008).

Before satellites came into practice, S was measured from sparse surveying ships

and tide gauge stations located along irregular local coastline. However, $\hat{N}$ was not easy

65   to observe. Without satellite measurements, the marine geoid is defined as the ***average***

level of SSH if the water is at rest and denoted here by N, which is called the classical

marine geoid (or first type marine geoid) (Fig. 1a). The first type marine geoid can be taken

as *a standalone concept in oceanography* since it is on the base of the hypothesis (mean

SSH when the water at rest) without using the gravity anomaly. In this framework, the

70   geostrophic balance

$$u_g = -\frac{1}{f\hat{\rho}}\frac{\partial \hat{p}}{\partial y}, \quad v_g = \frac{1}{f\hat{\rho}}\frac{\partial \hat{p}}{\partial x}, \tag{8}$$

and hydrostatic balance,

$$\frac{\partial \hat{p}}{\partial z} = -\hat{\rho}g, \tag{9}$$

are used for large-scale (i.e., scale > 100 km) processes. Here (u_g, v_g) are geostrophic

75   current components; f is the Coriolis parameter; $(\hat{p}, \hat{\rho})$ are in-situ pressure and density,

respectively, which can be decomposed into

$$\hat{\rho} = \rho_0 + \overline{\rho}(z) + \rho, \quad \hat{p} = -\rho_0 gz + \overline{p}(z) + p. \tag{10}$$

Here, $\rho_0 = 1025$ kg/m^3, is the characteristic density; $(\overline{\rho}, \overline{p})$ are horizontally uniform with

$\overline{\rho}$ vertically increasing with depth (stable stratification)

80

$$\partial\overline{\rho}/\partial z \equiv -\rho_0[n(z)]^2/g, \tag{11}$$

where $n(z)$ is the buoyancy frequency (or called the Brunt-Vaisala frequency); (p, ρ) are

anomalies of pressure and density. Near the ocean surface, it is common to use the

characteristic density and corresponding pressure (p_0, ρ_0) to represent $(\hat{p}, \hat{\rho})$. Vertical

integration of (9) from N to S after replacing $(\hat{p}, \hat{\rho})$ by (p_0, ρ_0) in (8) and (9) leads to

85

$$u_g(S) - u_g(N) = -\frac{g}{f}\frac{\partial D}{\partial y}, \quad v_g(S) - v_g(N) = \frac{g}{f}\frac{\partial D}{\partial x}, \tag{12}$$

where

$$D = S - N, \tag{13}$$

is the first type DOT. Since the first type marine geoid (N) is defined as the *average level of SSH if the water is at rest*,

90
$$u_g(N) = 0, \quad v_g(N) = 0,\qquad\qquad(14)$$

the horizontal gradient of D represents the **absolute surface geostrophic currents**.

After satellites came into practice, SSH has been observed with high precision and unique resolution with altimetry above a reference ellipsoid (not geoid) (Fu and Haines 2013). Two Gravity Recovery and Climate Experiment (GRACE) satellites, launched in
95 2002, provide data to compute the marine geoid [called the GRACE Gravity Model (GGM)] (see website: http://www.csr.utexas.edu/grace/) (Tapley et al., 2003; Shum et al., 2011). In addition, European Space Agency's GOCE mission data, along with the GRACE data, have produced the best mean gravity field or the geoid model at a spatial scale longer than 67 km half-wavelength (or spherical harmonics completed to degree 300). This marine
100 geoid is the solution of Eq(6),

$$\frac{\partial^2 N_*}{\partial x^2} + \frac{\partial^2 N_*}{\partial y^2} = \frac{1}{g}\frac{\partial(\Delta g)}{\partial z}$$

where N_* is the satellite determined marine geoid from the measurable gravity anomaly Δg, and called the second type marine geoid (Fig. 1b), which is different from N, defined by (14). Correspondingly, the second type DOT is defined by

105
$$D_* = S - N_*(t),\qquad\qquad(15)$$

where $N_*(t)$ changes with time due to temporally varying gravity anomaly Δg. Thus, comparison between the first-type and second-type geoids should be conducted between N and $\bar{N}_*$. Here, $\bar{N}_*$ is the temporally mean of $N_*(t)$. As for DOT, the first type DOT (D) should be compared to the second type mean DOT (MDOT),

110
$$\bar{D}_* = S - \bar{N}_*. \tag{16}$$

The oceanic conditions at N and $\bar{N}_*$ are different: water at rest on N [see Eq(14)], but in motion on $\bar{N}_*$. The oceanographic community ignores such a difference. The horizontal gradients of the second type DOT are also treated as the absolute surface geostrophic currents. For example, the second type MDOT ($\bar{D}_*$) data is posted at the

115 NASA/JPL website: https://grace.jpl.nasa.gov/data/get-data/dynamic-ocean-typography/. Its horizontal gradients are also taken as the absolute surface geostrophic currents.

A question arises: Do the horizontal gradients of the second type MDOT ($\bar{D}_*$) represent the *absolute surface geostrophic currents*? This paper will answer the question using the temporally averaged SSH and marine geoid from NASA's satellite altimetric and

120 gravimetric measurements [i.e., the second type MDOT ($\bar{D}_*$)], and solving a new elliptic equation of D numerically. Given (S, $\bar{N}_*$, D) leads to the answer of the question.

Rest of the paper is outlined as follows. Section 2 describes the change of DOT due to the change of marine geoid from first to second type. Section 3 describes geostrophic currents and energy related to the first type DOT. Section 4 presents the governing equation

125 of the first type DOT with the boundary condition at the coasts. Section 5 shows the numerical solution for the world oceans. Section 6 evaluates the change of global DOT from first to second type with oceanographic implication. Section 7 concludes the studies.

2. Change of DOT from first to second type

The second type MDOT ($\bar{D}_*$) data are downloaded from the NASA/JPL website:

130 https://grace.jpl.nasa.gov/data/get-data/dynamic-ocean-typography/. This dataset is subtraction of a second type marine geoid of GRACE (Bingham et al, 2011) from a mean

(1993 to 2006) altimetric sea surface. Change of marine geoid from first (N) to second ($\bar{N}_*$) type is represented by

$$\Delta N = \bar{N}_* - N . \tag{17}$$

135   Correspondingly, change of DOT is given by

$$\Delta D = \bar{D}_* - D = -\Delta N \tag{18}$$

where (13) and (16) are used. ΔD is of interest in oceanography. ΔN is of interest in geodesy. Eq(18) shows that the key issue to evaluate ΔD is to determine D (i.e., first type DOT).

140   Conservation of potential vorticity for a dissipation-free fluid does not apply precisely to sea water where the density is a function not only of temperature and pressure but also of the dissolved salts. The effect of salinity on density is very important in the distribution of water properties. However, for most dynamic studies the effect of the extra state variable is not significant and the conservation of potential vorticity is valid (Veronis, 145   1980). Based on the conservation of the potential vorticity, the geostrophic current reaches the minimum energy state (Appendix A). Due to the minimum energy state, an elliptic partial differential equation for D is derived with coefficients containing sea-floor topography H, and forcing function containing temperature and salinity fields.

    If ΔD is negligible in comparison to D, change of marine geoid from N to $\bar{N}_*$ does 150   not change absolute DOT's oceanographic interpretation, i.e., the horizontal gradients of $\bar{D}_*$ also represent the absolute surface geostrophic currents. If ΔD is not negligible, the horizontal gradient of $\bar{D}_*$ does not represent the absolute surface geostrophic currents.

3. Geostrophic currents and energy

Eq.(10) implies,

155

$$\frac{\partial \hat{\rho}}{\partial x} = \frac{\partial \rho}{\partial x}, \quad \frac{\partial \hat{\rho}}{\partial y} = \frac{\partial \rho}{\partial y}, \tag{19}$$

$$\frac{\partial \hat{p}}{\partial x} = \frac{\partial p}{\partial x}, \quad \frac{\partial \hat{p}}{\partial y} = \frac{\partial p}{\partial y}. \tag{20}$$

Using the first type marine geoid *N*, the horizontal gradients of *D* lead to the absolute surface geostrophic currents [see Eqs(12) and (14)]. Integration of the thermal wind relation

160

$$\frac{\partial u_g}{\partial z} = \frac{g}{f \rho_0} \frac{\partial \rho}{\partial y}, \quad \frac{\partial v_g}{\partial z} = -\frac{g}{f \rho_0} \frac{\partial \rho}{\partial x}, \tag{21}$$

from the ocean surface to depth *z* leads to depth-dependent geostrophic currents,

$$u_g(z) = u_g(S) + u_{BC}(z), \quad v_g(z) = v_g(S) + v_{BC}(z) \tag{22}$$

where

$$u_{BC}(z) = -\frac{g}{f \rho_0} \int_z^0 \frac{\partial \rho}{\partial y} dz', \quad v_{BC}(z) = \frac{g}{f \rho_0} \int_z^0 \frac{\partial \rho}{\partial x} dz', \tag{23}$$

165   are the baroclinic geostrophic currents. Here, $f = 2\Omega \sin(\varphi)$ is the Coriolis parameter; $\Omega = 2\pi/(86400 \text{ s})$ is the mean Earth rotation rate; φ is the latitude.

The volume integrated total energy, i.e., sum of kinetic energy of the geostrophic currents and the available potential energy (Oort et al., 1989), for an ocean basin (*W*) is given by

170

$$E = \iiint_W \left[\frac{1}{2} (u_g^2 + v_g^2) + \frac{g^2 \rho^2}{2 \rho_0^2 n^2} \right] dxdydz. \tag{24}$$

Substitution of (22) and (23) into (24) leads to

$$E(D_x, D_y, \rho) = \frac{g^2}{2} \iiint\limits_W \left[(-D_y + \frac{fu_{BC}}{g})^2 / f^2 + (D_x + \frac{fv_{BC}}{g})^2 / f^2 + \frac{\rho^2}{\rho_0^2 n^2} \right] dxdydz$$

$$= \frac{g^2}{2} \iiint\limits_W \left[D_x^2 / f^2 + D_y^2 / f^2 + 2D_x \frac{v_{BC}}{fg} - 2D_y \frac{u_{BC}}{fg} \right] dxdydz$$

$$+ \frac{1}{2} \iiint\limits_W \left[u_{BC}^2 + v_{BC}^2 + \frac{g^2 \rho^2}{\rho_0^2 n^2} \right] dxdydz \tag{25}$$

4. Governing equation of D

175   For a given density field, the second integration in the right side of (25) is known. The

geostrophic currents taking the minimum energy state provides a constraint for D,

$$G(D_x, D_y) \equiv \iiint\limits_W \left[\left(D_x^2 + D_y^2 + 2D_x \frac{fv_{BC}}{g} - 2D_y \frac{fu_{BC}}{g} \right) / f^2 \right] dxdydz \rightarrow \min. \tag{26}$$

The three-dimensional integration (26) over the ocean basin is conducted by

$$\iiint\limits_W [...] dxdydz = \iint\limits_R \left\{ \int\limits_{-H}^0 [...] dz \right\} dxdy \tag{27}$$

180   where R is the horizontal area of the water volume, H is the water depth. Thus, Eq(26)

becomes

$$G(D_x, D_y) = \iint\limits_R L(D_x, D_y) dxdy \rightarrow \min, \tag{28}$$

$$L(D_x, D_y) \equiv \left[H(D_x^2 + D_y^2) + 2D_x Y - 2D_y X \right] / f^2 \tag{29}$$

where the parameters (X, Y) are given by

185    $$X(x, y) \equiv \frac{f}{g} \int\limits_{-H}^0 u_{BC} dz = -\frac{1}{\rho_0} \int\limits_{-H}^0 \int\limits_z^0 \frac{\partial \hat{\rho}}{\partial y} dz' dz \tag{30}$$

$$Y(x, y) \equiv \frac{f}{g} \int\limits_{-H}^0 v_{BC} dz = \frac{1}{\rho_0} \int\limits_{-H}^0 \int\limits_z^0 \frac{\partial \hat{\rho}}{\partial x} dz' dz, \tag{31}$$

which represent vertically integrated baroclinic geostrophic currents scaled by the factor

f/g (unit: m). Here, Eq.(19) is used (i.e., horizontal gradient of in-situ density is the same

as that of density anomaly).

190   The Euler-Lagragian equation of the functional (28) is given by

$$\frac{\partial L}{\partial D} - \frac{\partial}{\partial x}\left(\frac{\partial L}{\partial D_x}\right) - \frac{\partial}{\partial y}\left(\frac{\partial L}{\partial D_y}\right) = 0 . \qquad (32)$$

Substitution of (29) into (32) gives an elliptic partial differential equation (i.e., the

governing equation) for the first type DOT (i.e., D),

$$f^2 \nabla \left[\left(H / f^2\right)\nabla D\right] = -F,$$

195   or

$$\boxed{H\left[\nabla^2 D + r^{(x)}\frac{\partial D}{\partial x} + r^{(y)}\frac{\partial D}{\partial y} - 2(\beta / f)\frac{\partial D}{\partial y}\right] = -F} , \qquad (33)$$

where

$$F \equiv \left(\frac{\partial Y}{\partial x} - \frac{\partial X}{\partial y}\right), \quad \nabla \equiv \mathbf{i}\frac{\partial}{\partial x} + \mathbf{j}\frac{\partial}{\partial y} \qquad (34)$$

$$r^{(x)} \equiv \frac{1}{H}\frac{\partial H}{\partial x}, \quad r^{(y)} \equiv \frac{1}{H}\frac{\partial H}{\partial y}, \quad \beta = \frac{2\Omega}{a}\cos(\varphi), \qquad (35)$$

200   where $a = 6,370$ km, is the mean earth radius. The geostrophic balance does not exist at the

equator. The Coriolis parameter f needs some special treatment for low latitudes. In this

study, f is taken as $2\Omega\sin(5\pi/180)$ if latitude between 10ºN to 0º; and as

$-2\Omega\sin(5\pi/180)$ if latitude between 0º to 10ºS.

Let Γ be the coastline of ocean basin. Continuation of geoid from land to oceans

205   gives

$$N|_\Gamma = N_l|_\Gamma, \quad \bar{N}_*|_\Gamma = N_l|_\Gamma, \tag{36}$$

which leads to

$$N|_\Gamma = \bar{N}_*|_\Gamma. \tag{37}$$

Here, N_l is the geoid over land. The boundary condition (37) can be rewritten as

210
$$\boxed{D|_\Gamma = (S - N)|_\Gamma = (S - \bar{N}_*)|_\Gamma = \bar{D}_*|_\Gamma} \tag{38}$$

which is boundary condition of D.

5. Numerical solution of D

The well-posed elliptic equation (33) is integrated numerically on $1^\circ \times 1^\circ$ grids for the world

oceans with the boundary values [i.e., (38)] taken from the MDOT (1993-2006) field (i.e.,

215   $\bar{D}_*$), at the NASA/JPL website: https://grace.jpl.nasa.gov/data/get-data/dynamic-ocean-

typography/ (0.5° interpolated into 1° resolution). The forcing function F is calculated on

$1^\circ \times 1^\circ$ grid from the World Ocean Atlas 2013 (WOA13) temperature and salinity fields,

which was downloaded from the NOAA National Centers for Environmental Information

(NCEI) website: https://www.nodc.noaa.gov/OC5/woa13/woa13data.html. The three

220   dimensional density was calculated using the international thermodynamic equation of

seawater   -2010,   which   is   downloaded   from   the   website:

http://unesdoc.unesco.org/images/0018/001881/188170e.pdf.   The   ocean   bottom

topography data H was downloaded from the NECI 5-Minute Gridded Global Relief Data

Collection   at   the   website: https://www.ngdc.noaa.gov/mgg/fliers/93mgg01.html.

225   Discretization of the elliptic equation (33) and numerical integration are given in Appendix

B.

6. Difference between the Two DOTs

The first type global DOT (D_{ij}) (Fig. 2a) is the numerical solution of the elliptic equation (33) with the boundary condition (38). The second type global MDOT ($\bar{D}_{*ij}$) (Fig. 2b) is downloaded from the NASA/JPL website: https://grace.jpl.nasa.gov/data/get-data/dynamic-ocean-typography/. Difference between the two DOTs,

$$\Delta D_{ij} = \bar{D}_{*ij} - D_{ij}, \tag{39}$$

is evident in the world oceans (Fig. 2c). Here, (i, j) denote the horizontal grid point. The relative root-mean-square (RMS) of ΔD is given by

$$\text{RRMS}(\Delta D) = \frac{\sqrt{\frac{1}{M}\sum_i\sum_j(\Delta D_{ij})^2}}{\sqrt{\frac{1}{M}\sum_i\sum_j(D_{ij})^2}} = 0.386. \tag{40}$$

where M = 38,877 is the number of total grid points. Both D and $\bar{D}_*$ have positive and negative values. The arithmetic mean values (0.524 cm, -3.84 cm) are much smaller than the RMS mean values. They are an order of magnitude smaller than the corresponding standard deviations (54.9 cm, 71.2 cm) (see Figs. 2d and 2e). The magnitudes of D and $\bar{D}_*$ are represented by their root-mean squares, which are close to their standard deviations.

Histograms of for D_{ij} (Fig. 2d) and $\bar{D}_{*ij}$ (Fig. 2e) are both non-Gaussian and negatively skewed. The major difference between the two is the single modal for D_{ij} with a peak at around 20 cm and the bi-modal for $\bar{D}_{*ij}$ with a high peak at around 30 cm and a low peak at -140 cm. The statistical parameters are different, such as mean value and standard deviation are (0.524 cm, 54.9 cm) for D_{ij}, and (-3.84 cm, 71.2 cm) for $\bar{D}_{*ij}$. Skewness and kurtosis are (-0.83, 3.01) for D_{ij}, and (-0.87, 2.80) for $\bar{D}_{*ij}$.

Horizontal gradients of the DOT, ($\partial D_{ij}/\partial x$, $\partial D_{ij}/\partial y$) and ($\partial \bar{D}_{*ij}/\partial x$, $\partial \bar{D}_{*ij}/\partial y$), have oceanographic significance (i.e., related to the geostrophic currents). They are calculated using the central difference scheme at inside-domain grid points and the first order forward/backward difference scheme at grid points next to the boundary. Difference in global $\partial D_{ij}/\partial x$ (Fig. 3a) and $\partial \bar{D}_{*ij}/\partial x$ (Fig. 3b) is evident with much smaller-scale structures in $\partial \bar{D}_{*ij}/\partial x$. The difference between the two gradients (Fig. 3c),

$$\Delta(\partial D_{ij}/\partial x) = \partial \bar{D}_{*ij}/\partial x - \partial D_{ij}/\partial x \qquad (41)$$

has the same order of magnitudes as the gradients themselves with the relative root-mean-square (RMS) of $\Delta(\partial D/\partial x)$,

$$\mathrm{RRMS}\left[\Delta(\partial D/\partial x)\right] = \frac{\sqrt{\dfrac{1}{M}\sum_i\sum_j\left[\Delta(\partial D_{ij}/\partial x)\right]^2}}{\sqrt{\dfrac{1}{M}\sum_i\sum_j(\partial D_{ij}/\partial x)^2}} = 1.04\,, \qquad (42)$$

which implies that the non-surface latitudinal geostrophic current component of the second type MDOT has the same order of magnitude as the surface latitudinal geostrophic current component of the first type DOT. Histograms of for $\partial D_{ij}/\partial x$ (Fig. 3d) and $\partial \bar{D}_{*ij}/\partial x$ (Fig. 3e) are near symmetric with mean values around (-1.29, -0.78)×10⁻⁸ and standard deviations (2.69, 4.95)×10⁻⁷. The standard deviation of $\partial \bar{D}_{*ij}/\partial x$ is almost twice that of $\partial D_{ij}/\partial x$.

Similarly, difference in global $\partial D_{ij}/\partial y$ (Fig. 4a) and $\partial \bar{D}_{*ij}/\partial y$ (Fig. 4b) is evident with much smaller-scale structures in $\partial \bar{D}_{*ij}/\partial y$. The difference between the two gradients (Fig. 4c),

$$\Delta(\partial D_{ij} / \partial y) = \partial \bar{D}_{*ij} / \partial y - \partial D_{ij} / \partial y \qquad (43)$$

has the same order of magnitudes as the gradients themselves with the relative root-mean-square (RMS) of $\Delta(\partial D / \partial y)$,

$$\mathrm{RRMS}\left[\Delta(\partial D / \partial y)\right] = \frac{\sqrt{\dfrac{1}{M}\displaystyle\sum_{i}\sum_{j}\left[\Delta(\partial D_{ij} / \partial y)\right]^2}}{\sqrt{\dfrac{1}{M}\displaystyle\sum_{i}\sum_{j}(\partial D_{ij} / \partial y)^2}} = 0.98, \qquad (44)$$

270   which implies that the non-surface zonal geostrophic current component of the second type MDOT has the same order of magnitude as the surface zonal geostrophic current component of the first type DOT.   Histograms of $\partial D_{ij}/\partial y$ (Fig. 4d) and $\partial \bar{D}_{*ij} / \partial y$ (Fig. 4e) are also near symmetric with the mean values around $(2.32, 1.18)\times 10^{-7}$ and standard deviations $(1.20, 2.44)\times 10^{-6}$.   The standard deviation of $\partial \bar{D}_{*ij} / \partial y$ is almost twice that of

275   $\partial D_{ij}/\partial y$. The denominators of (42) and (44) represent the magnitudes of the horizontal gradients of the first type DOT.

7. Conclusions

Change of marine geoid from classical defined (first type, standalone concept in oceanography) to satellite determined (second type, *standalone concept in marine geodesy*)

280   largely affects oceanography. With the classical defined marine geoid (***average level of SSH if the water is at rest***) the horizontal gradients of the first type DOT represent the absolute surface geostrophic currents. With the satellite determined (second type) marine geoid by Eq(6), the horizontal gradients of the second type MDOT don't represent the absolute surface geostrophic currents. The difference between the two types of DOT

285   represents an additional component to the absolute surface geostrophic currents.

14

With conservation of potential vorticity, geostrophic balance represents the minimum energy state in an ocean basin where the mechanical energy is conserved. A new governing elliptic equation of first type DOT is derived with water depth (H) in the coefficients and the three dimensional temperature and salinity in the forcing function. This governing elliptic equation is well posed. Continuation of geoid from land to ocean leads to an inhomogeneous Dirichlet boundary condition.

Difference between the two types of DOT is evident with relative root-mean-square difference of 38.6%. Horizontal gradients (representing geostrophic currents) of the two type DOTs are different with much smaller-scale structures in the second type absolute DOT. Relative root-mean-square difference is near 1.0 in both (x, y) components of the DOT gradient, which implies that the non-absolute surface geostrophic currents identified from the second type has the same order of magnitudes of the absolute surface geostrophic currents identified by the first type DOT.

The notable difference between the two types of DOT raises more questions in oceanography and marine geodesy: Is there any theoretical foundation to connect the classical marine geoid (*standalone concept in oceanography* using the principle of surface geostrophic currents without Δg) to the satellite determined marine geoid (*standalone concept in marine geodesy* using Δg without the principle of surface geostrophic currents)? How can the satellite determined marine geoid using the gravity anomaly (Δg) be conformed to the basic physical oceanography principle of surface geostrophic currents? What is the interpretation of the horizontal gradients of the second type MDOT ($\bar{D}_*$)? Is there any evidence or theory to show $[u_g(\bar{N}_*) = 0, \ v_g(\bar{N}_*) = 0]$ similar to Eq.(14)? More observational and theoretical studies are needed in order to solve those problems. The

main challenge for oceanographers is how to use the satellite altimetry observed SSH such

310 as the Surface Water and Ocean Topography (SWOT, https://swot.jpl.nasa.gov/) to infer

the ocean general circulations at the surface. A new theoretical framework rather than the

geostrophic constraint needs to be established.

The GOCE determined satellite data-only geoid model is more accurate and with

higher resolution than GRACE. Change of GRACE to GOCE geoid model may increase

315 the accuracy of the calculation of the second type DOT. However, such a replacement does

not solve the fundamental problem presented here, i.e., incompatibility between satellite

determined marine geoid using the gravity anomaly (Δg) and the classical marine geoid

(mean SSH when the water at rest) on the base of the basic physical oceanography principle

of surface geostrophic currents.

320 Finally, the mathematical framework described here [i.e., the elliptic equation (33)

with boundary condition (38)] may lead to a new inverse method for calculating three-

dimensional absolute geostrophic velocity from temperature and salinity fields since the

surface absolute geostrophic velocity is the solution of (33). This will be a useful addition

to the existing β-spiral method (Stommel and Schott, 1977), box model (Wunsch, 1978),

325 and P-vector method (Chu, 1995; Chu et al., 1998, 2000).

Appendix A. Geostrophic balance as a minimum energy state in an

330 **energy conserved basin**

16

In large scale motion (small Rossby number) with the Boussinesq approximation, the linearized PV (Π) is given by

$$\Pi \approx [f + (\frac{\partial v}{\partial x} - \frac{\partial u}{\partial y})]\frac{\partial \hat{\rho}}{\partial z} \approx f(-\frac{\rho_0 n^2}{g} + \frac{\partial \rho}{\partial z}) - \frac{\rho_0 n^2}{g}(\frac{\partial v}{\partial x} - \frac{\partial u}{\partial y}). \qquad (A1)$$

where, $\rho_0 = 1025$ kg m^{-3} is the characteristic density. Without the frictional force and zero
335   horizontally integrated buoyancy flux at the surface and bottom, the energy (including kinetic and available potential energies) is conserved in a three dimensional ocean basin (V)

$$E = \iiint_V J dx dy dz, \quad J \equiv \frac{1}{2}(u^2 + v^2 + w^2) + \frac{g^2 \rho^2}{2\rho_0^2 n^2}, \qquad (A2)$$

$$\frac{dE}{dt} = 0 \qquad (A3)$$

340   The two terms of J are kinetic energy, and available potential energy.

     To show the geostrophic balance taking the minimum energy state for a given linear PV [see (A1)], the constraint is incorporated by extremizing the integral (see also in Vallis 1992; Chu 2018)

$$I \equiv \iiint_V \left\{ \begin{array}{l} \frac{1}{2}(u^2 + v^2 + w^2) + \frac{g^2 \rho^2}{2\rho_0^2 n^2} \\ +\mu(x,y,z)\left[f(-\frac{\rho_0 n^2}{g} + \frac{\partial \rho}{\partial z}) - \frac{\rho_0 n^2}{g}(\frac{\partial v}{\partial x} - \frac{\partial u}{\partial y}) \right] \end{array} \right\} dx dy dz \qquad (A4)$$

345   where $\mu(x, y, z)$ is the Lagrange multiplier, which is a function of space. If it were a constant, the integral would merely extremize energy subject to a given integral of PV, and rearrangement of PV would leave the integral unaltered. Extremization of the integral (A4) gives the three Euler-Lagrange equations,

17

$$\frac{\partial K}{\partial \rho} - \frac{\partial}{\partial z}\frac{\partial K}{\partial \rho_z} = 0, \tag{A5}$$

$$\frac{\partial K}{\partial u} - \frac{\partial}{\partial y}\frac{\partial K}{\partial u_y} = 0, \tag{A6}$$

$$\frac{\partial K}{\partial v} - \frac{\partial}{\partial x}\frac{\partial K}{\partial v_x} = 0. \tag{A7}$$

where K is in the integrand appearing in (A4). Substitution of K into (A5), (A6), (A7) leads to

$$\frac{g^2}{\rho_0^2 n^2}\rho = f\frac{\partial \mu}{\partial z}, \tag{A8}$$

$$u = \frac{\rho_0 n^2}{g}\frac{\partial \mu}{\partial y}, \quad v = -\frac{\rho_0 n^2}{g}\frac{\partial \mu}{\partial x}. \tag{A9}$$

Differentiation of (A9) with respect to z and use of (A8) leads to

$$\frac{\partial u}{\partial z} = \frac{g}{f\rho_0}\frac{\partial \rho}{\partial y} = \frac{\partial u_g}{\partial z}, \quad \frac{\partial v}{\partial z} = -\frac{g}{f\rho_0}\frac{\partial \rho}{\partial x} = \frac{\partial v_g}{\partial z}, \tag{A10}$$

which shows that $(u, v) = (u_g, v_g)$ have the minimum energy state.

Appendix B. Numerical solution of the equation (33)

Let the three axes (x, y, z) be discretized into local rectangular grids in horizontal and non-uniform grids in vertical $(x_{i,j}, y_{i,j}, z_k)$ with cell sizes $(1°\times1°)$,

$$\Delta y = \frac{\pi}{360}\mathrm{r}_E, \ \Delta x_j = \Delta y \cos\phi_j, \ \Delta z_k = z_k - z_{k+1},$$

$$i = 1, 2, \dots, I; \ j = 1, 2, \dots, J; \ k = 1, 2, \dots, K_{i,j} \tag{B1}$$

where $k = 1$ for the surface, $k = K_{ij}$ for the bottom; ϕ_j is the latitude of the grid point; $\mathrm{r}_E = 6{,}371$ km, is the earth radius; $I = 360$; $J = 180$. The subscripts in $K_{i,j}$ in (B1) indicates non-uniform water depth in the region.

18

The parameters $(X_{i,j}, Y_{i,j})$ in (30) and (31) (in Section 4) are calculated by

$$X_{i,j} \equiv \frac{1}{4\rho_0} \sum_{k=2}^{K_{i,j}} \sum_{l=1}^{k} \left[\left(\frac{\hat{\rho}_{i,j+1,l} - \hat{\rho}_{i,j,l}}{\Delta y} + \frac{\hat{\rho}_{i+1,j+1,l} - \hat{\rho}_{i+1,j,l}}{\Delta y} \\ + \frac{\hat{\rho}_{i,j+1,l+1} - \hat{\rho}_{i,j,l+1}}{\Delta y} + \frac{\hat{\rho}_{i+1,j+1,l+1} - \hat{\rho}_{i+1,j,l+1}}{\Delta y} \right) \Delta z_k \left(\frac{\Delta z_l + \Delta z_{l+1}}{2} \right) \right] \quad \text{(B2)}$$

$$Y_{i,j} \equiv \frac{1}{4\rho_0} \sum_{k=2}^{K_{i,j}} \sum_{l=1}^{k} \left[\left(\frac{\hat{\rho}_{i+1,j,l} - \hat{\rho}_{i,j,l}}{\Delta x_j} + \frac{\hat{\rho}_{i+1,j+1,l} - \hat{\rho}_{i,j+1,l}}{\Delta x_j} \\ + \frac{\hat{\rho}_{i+1,j,l+1} - \hat{\rho}_{i,j,l+1}}{\Delta x_j} + \frac{\hat{\rho}_{i+1,j+1,l+1} - \hat{\rho}_{i,j+1,l+1}}{\Delta x_j} \right) \Delta z_k \left(\frac{\Delta z_l + \Delta z_{l+1}}{2} \right) \right] \quad \text{(B3)}$$

370   which gives the discretized forcing function

$$F_{i,j} = \frac{Y_{i+1,j} - Y_{i-1,j}}{2\Delta x_j} - \frac{X_{i,j+1} - X_{i,j-1}}{2\Delta y} \quad \text{(B4)}$$

The governing equation (33) is discretized by

$$\frac{D_{i+1,j} - 2D_{i,j} + D_{i-1,j}}{(\Delta x_j)^2} + \frac{D_{i,j+1} - 2D_{i,j} + D_{i,j-1}}{(\Delta y)^2} \\ + r_{ij}^{(x)} \frac{D_{i+1,j} - D_{i-1,j}}{2\Delta x_j} + \left(r_{ij}^{(y)} - \frac{2\beta_j}{f_j} \right) \frac{D_{i,j+1} - D_{i,j-1}}{2\Delta y} = -\frac{F_{ij}}{H_{ij}} \quad \text{(B5)}$$

which is reorganized by

$$2(1 + \cos^2 \phi_j) D_{i,j} = (1 + \frac{1}{2} r_{ij}^{(x)} \Delta y \cos \phi_j) D_{i+1,j} + (1 - \frac{1}{2} r_{ij}^{(x)} \Delta y \cos \phi_j) D_{i-1,j}$$

375    $$+ \cos^2 \phi_j \left[1 + \left(r_{ij}^{(y)} - \frac{2 \cot \phi_j}{r_E} \right) \frac{\Delta y}{2} \right] D_{i,j+1} + \cos^2 \phi_j \left[1 - \left(r_{ij}^{(y)} - \frac{2 \cot \phi_j}{r_E} \right) \frac{\Delta y}{2} \right] D_{i,j-1} \quad \text{(B6)}$$

$$+ \frac{F_{ij}}{H_{ij}} (\Delta y)^2 \cos^2 \phi_j$$

The iteration method is used to solve the algebraic equation (B6) with large value of $I \times J$.

It starts from the 0-step,

$$D_{ij}^{(0)} = 0, \quad i = 1, 2, \ldots, I; \; j = 1, 2, \ldots, J \quad \text{(B7)}$$

19

With the given boundary condition (38) (see Section 4) and forcing function (B4), the first type DOT at the grid points can be computed from steps n to $n+1$,

$$2(1+\cos^2\phi_j)D_{ij}^{(n+1)} = (1+\frac{1}{2}r_{ij}^{(x)}\Delta y\cos\phi_j)D_{i+1,j}^{(n)} + (1-\frac{1}{2}r_{ij}^{(x)}\Delta y\cos\phi_j)D_{i-1,j}^{(n)}$$
$$+\cos^2\phi_j\left[1+\left(r_{ij}^{(y)}-\frac{2\cot\phi_j}{r_E}\right)\frac{\Delta y}{2}\right]D_{i,j+1}^{(n)} + \cos^2\phi_j\left[1-\left(r_{ij}^{(y)}-\frac{2\cot\phi_j}{r_E}\right)\frac{\Delta y}{2}\right]D_{i,j-1}^{(n)} + \frac{F_{ij}}{H_{ij}}(\Delta y)^2\cos^2\phi_j$$

(B8)

Such iteration continues until the relative root-mean square difference reaching the criterion,

$$r = \frac{\sqrt{\frac{1}{M}\sum_{i=1}^{I}\sum_{j=1}^{J}\left[D_{ij}^{(n+1)}-D_{ij}^{(n)}\right]^2}}{\sqrt{\frac{1}{M}\sum_{i=1}^{I}\sum_{j=1}^{J}\left[D_{ij}^{(n)}\right]^2}} < 10^{-6},$$

(B9)

where $M = 38,877,$ is the total number of the grid points on the ocean surface.

References

Bingham, R.J., Haines, K., & Hughes, C.W. (2008). Calculating the ocean's mean dynamic topography from a mean sea surface and a geoid. *J. Atmos. Oceanic Technol.*, **25**, 1808-1822.

Chu, P.C. (1995). P-vector method for determining absolute velocity from hydrographic data. *Mar. Tech. Soc. J.*, **29** (3), 3-14.

Chu, P.C., Fan, C.W., Lozano, C.J., & Kerling, J. (1998). An AXBT survey of the South China Sea. *J. Geophy. Res.*, **103**, 21637-21652.

Chu, P.C., & Li, R.F. (2000). South China Sea isopycnal surface circulations. *J. Phys. Oceanogr.*, **30**, 2419-2438.

Chu, P.C. (2018) Determination of dynamic ocean topography using the minimum energy state. *Univ. J. Geosci.*, **6** (2) 25-39, DOI 10 13189/uig.2018 060201.

405   Fu, L.-L., & Haines, B.J. (2013). The challenges in long-term altimetry calibration for addressing the problem of global sea level change. *Adv. Space Res*., **51** (8), 1284-1300.

Hofmann-Wellenhof, B. & Moritz, H., (2006). *Physical geodesy*, Springer, pp 388.

410   Oort, A.H., Acher, S.C., Levitus, S., & Peixoto, J.P. (1989). New estimates of the available potential energy in world ocean. *J. Geophys. Res*., **94**, 3187-3200.

Shum, C.K., Guo, J., Hossain, F., Duan, J., Alsdorf, D., Duan, X., Kuo, C., Lee, H., Schmidt, M., & Wang, L. (2011). Inter-annual water storage changes in Asia from GRACE
415   data, *Climate Change and Food Security in South Asia*, R. Lal, M. Sivakumar, S. Faiz, A. Rahman, and K. Islam (Eds.). Part 2, Chapter 6, 69-83, doi: 10.1007/978-90-481-9516-9_6.

Stommel, H., & Schott, F. (1977). The beta spiral and the determination of the absolute
420   velocity field from hydrographic station data. *Deep-Sea Res*., **24**: 325-329.

Tapley, B.D., Chambers, D.P., Bettadpur, S., & Ries, J.C. (2003). Large scale ocean circulation from the GRACE GGM01 geoid. *Geophys. Res. Lett*., **30**, 2163, doi:10.1029/2003GL018622.
425
Vallis, G.K. (1992). Mechanisms and parameterizations of geostrophic adjustment and a variational approach to balanced flow. *J. Atmos. Sci*., **49**, 1144-1160.

Veronis, G. (1980). Dynamics of large-scale ocean circulation, *in* Evolution of Physical
430   Oceanography, B. A. Warren and C. Wunsch, eds., M.I.T. Press, Cambridge, MA, 140–184.

Wunsch, C. (1978). The general circulation of the North Atlantic west of 50º W determined from inverse methods. *Rev. Geophys*. **16**: 583-620.
435
Wunsch, C., & Gaposchkin, E.M. (1980). On using satellite altimetry to determine the general circulation of the oceans with application to geoid improvement. *Rev. Geophys*., **18**, 725-745.

440   **Figure Captions**

Figure 1. Two types of marine geoid and DOT: (a) first type with N the average level of SSH if water at rest (classical definition), and (b) second type with satellite determined N_* (water in motion on N_*).

21

445   Figure 2. (a) First type DOT (i.e., D) which is the solution of (33) with boundary condition of (38) (unit: cm), (b) second type MDOT (1993-2006) (i.e., $\bar{D}_*$) (unit: cm) downloaded from the NASA/JPL website: https://grace.jpl.nasa.gov/data/get-data/dynamic-ocean-typography, (c) difference between the two DOTs (i.e., ΔD), (d) histogram of global D, and (e) histogram of global $\bar{D}_*$.

450

Figure 3. Derivatives in the x-direction of (a) the first type DOT (i.e., $\partial D/\partial x$), (b) the second MDOT (i.e., $\partial \bar{D}_* / \partial x$), (c) the difference $\Delta(\partial D / \partial x) = \partial \bar{D}_* / \partial x - \partial D / \partial x$, (d)

455   histogram of global $\partial D/\partial x$, and (e) histogram of global $\partial \bar{D}_* / \partial x$.

Figure 4. Derivatives in the y-direction of (a) the first type DOT (i.e., $\partial D/\partial y$), (b) the second type MDOT (i.e., $\partial \bar{D}_* / \partial y$), and (c) the difference $\Delta(\partial D / \partial y) = \partial \bar{D}_* / \partial y - \partial D / \partial y$, (d)

460   histogram of global $\partial D/\partial y$, and (e) histogram of global $\partial \bar{D}_* / \partial y$.
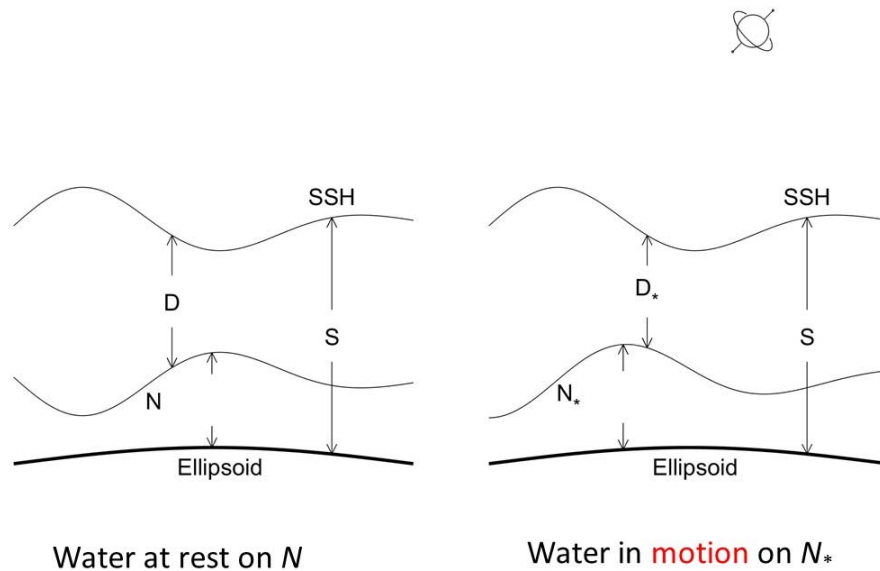
Figure 1. Two types of marine geoid and DOT: (a) first type with N the average level of SSH if water at rest (classical definition), and (b) second type with satellite determined N_*

465   (water in motion on N_*).

Figure 2. (a) First type DOT (i.e., D) which is the solution of (33) with boundary condition of (38) (unit: cm), (b) second type MDOT (1993-2006) (i.e., $\bar{D}_*$) (unit: cm) downloaded from the NASA/JPL website: https://grace.jpl.nasa.gov/data/get-data/dynamic-ocean-typography, (c) difference between the two DOTs (i.e., ΔD), (d) histogram of global D, and (e) histogram of global $\bar{D}_*$.
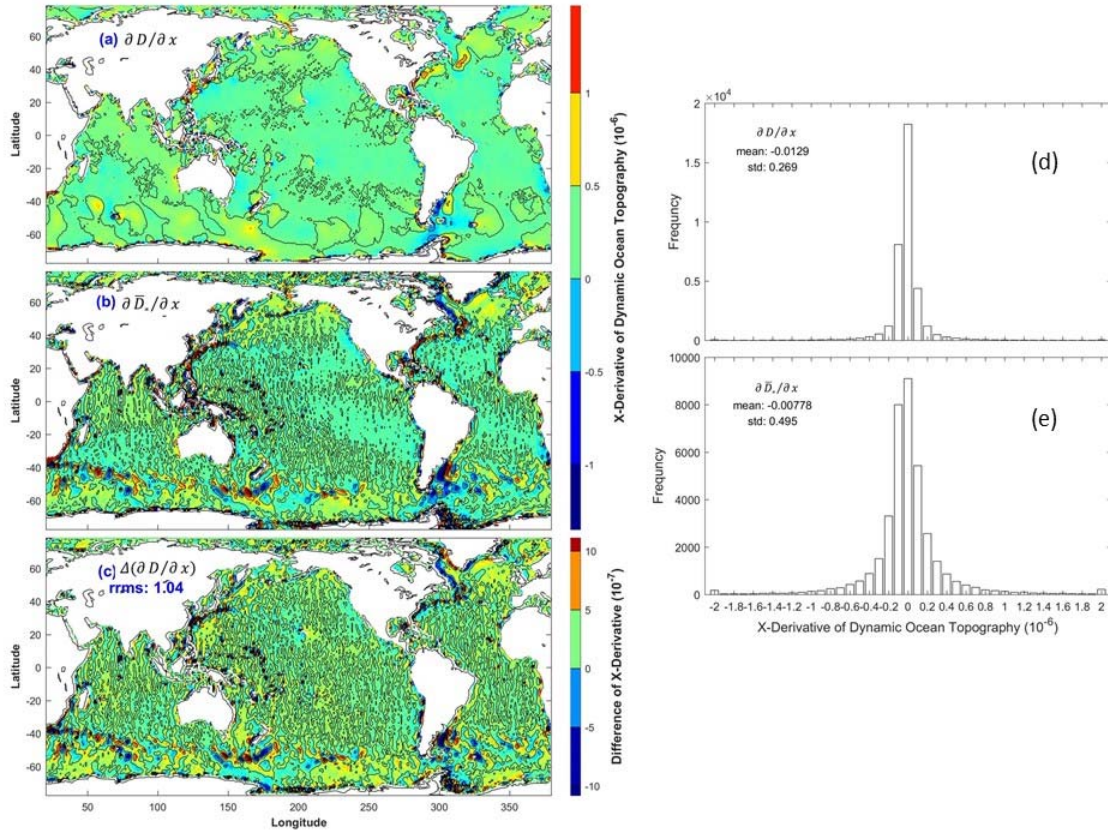
Figure 3. Derivatives in the *x*-direction of (a) the first type DOT (i.e., $\partial D/\partial x$), (b) the second MDOT (i.e., $\partial \bar{D}_* / \partial x$), (c) the difference $\Delta(\partial D / \partial x) = \partial \bar{D}_* / \partial x - \partial D / \partial x$, (d) histogram of global $\partial D/\partial x$, and (e) histogram of global $\partial \bar{D}_* / \partial x$.

480
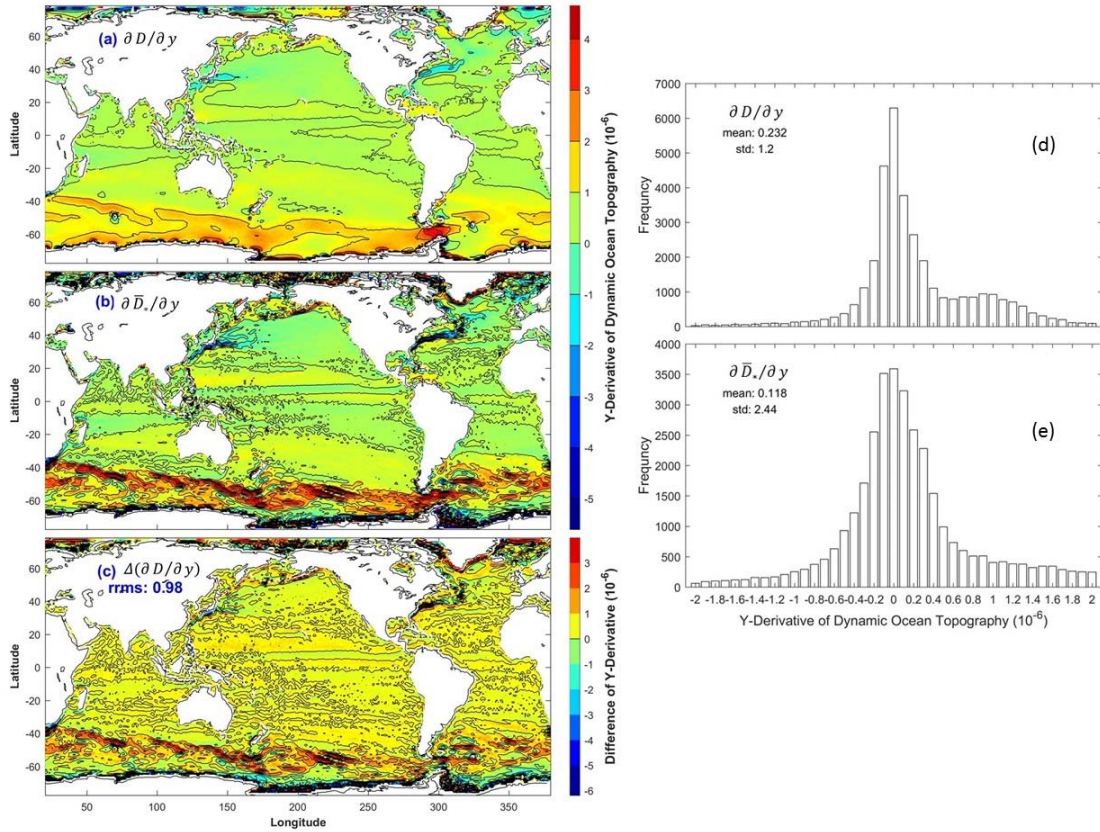
485   Figure 4. Derivatives in the *y*-direction of (a) the first type DOT (i.e., $\partial D/\partial y$), (b) the second type MDOT (i.e., $\partial \bar{D}_* / \partial y$), and (c) the difference $\Delta(\partial D / \partial y) = \partial \bar{D}_* / \partial y - \partial D / \partial y$, (d) histogram of global $\partial D/\partial y$, and (e) histogram of global $\partial \bar{D}_* / \partial y$.

490